Journal of Cleaner Production 279 (2021) 123408

Contents lists available at ScienceDirect

Journal of Cleaner Production

journal homepage: www.elsevier.com/locate/jclepro

Boosted bisphenol A and Cr(VI) cleanup over Z-scheme WO_3/MIL-100(Fe) composites under visible light

Jia-Wei Wang [a], Fu-Guo Qiu [a], Peng Wang [a], Chengjun Ge [b], Chong-Chen Wang [a, c, *]

[a] Beijing Key Laboratory of Functional Materials for Building Structure and Environment Remediation, School of Environment and Energy Engineering, Beijing University of Civil Engineering and Architecture, Beijing, 100044, China

[b] Key Laboratory of Agro-Forestry Environmental Processes and Ecological Regulation of Hainan Province, School of Ecology and Environment, Hainan University, Haikou, 570228, China

[c] College of Environmental Science and Engineering, North China Electric Power University, Beijing, 102206, China

ARTICLE INFO

Article history:
Received 28 January 2020
Received in revised form
18 July 2020
Accepted 21 July 2020
Available online 8 August 2020

Handling editor: Prof. Jiri Jaromir Klemeš

Keywords:
MIL-100(Fe)
WO_3
Cr(VI) reduction
Bisphenol A
Z-Scheme

ABSTRACT

To develop a new efficient catalyst for contaminant removal and sustainable environment, series Z-scheme WO_3/MIL-100(Fe) (M*x*W*y*) composites were easily prepared by ball-milling strategy, which were affirmed by various characterization techniques. All the as-prepared M*x*W*y* composites displayed superior photocatalytic Cr(VI) reduction and photo-Fenton bisphenol A(BPA) degradation performances under LED visible light, in which the M80W120 could accomplish 100% Cr(VI) reduction via photocatalysis treatment within 60 min and 100% BPA degradation with the aid of photo-Fenton process in 20 min. The influences of different initial pH, co-existing foreign ions, low weight organic molecules and H_2O_2 dosage on photocatalytic/photo-Fenton performances were clarified. Moreover, M80W120 displayed outstanding stability and reusability during five successive cycling experiments on Cr(VI) sequestration and BPA degradation, respectively. Also, the possible degradation pathway of BPA degradation over M80W120 was clarified. Finally, a Z-scheme mechanism was put forward, which was further confirmed by active species capture, photo-deposition of PbO_2 along with electron spin-resonance spectroscopy determination. The combination of MIL-100(Fe) and WO_3 was confirmed to be an effective strategy for pollutant removal and cleaner production.

1. Introduction

Nowadays, water pollution is becoming a focus issue, and has attracted more and more attention (Buaisha et al., 2020). Chromium is a representative heavy metal pollutant, and mainly comes from leather tanning, metallurgy, electroplating, paint pigments, textile production and other industries (Liang et al., 2015a, 2015b). In wastewater, the chromium mainly presents in the form of trivalent chromium (Cr(III)) with low toxicity and hexavalent chromium (Cr(VI)) with high toxicity (Debnath et al., 2016). The Cr(VI) can easily be absorbed in human body through the skin and respiratory tract, which can cause damage to the urinary tract, liver and kidney functions (Wang et al., 2015). Bisphenol A (BPA), as a typical endocrine disrupting chemicals (EDCs), has been widely used in plastic products and can coating (Zhang et al., 2014). BPA can exert great threat to human health, and can cause metabolism disorders and cancers. In addition, BPA has the effect of estrogen and can cause feminization even at a low-dose exposure, which has high risk to the health of baby and children (Molkenthin et al., 2013). In view of the potential threats of Cr(VI) and BPA, it is necessary to develop new materials to remove Cr(VI) and BPA from wastewater

Advanced oxidation processes (AOPs) like photocatalysis and photo-Fenton are considered to be cleaner technologies for pollutants removal, mainly due to their sustainability, high efficiency, low cost and high redox activities (Zhao et al., 2019). AOPs can produce some free radicals like •OH, which can non-selectively degrade the organic contaminants (Wu et al., 2020). Recently, metal-organic frameworks (MOFs), as emerging catalysts, have been widely applied in contaminants removal via photocatalysis and photo-Fenton processes. Their excellent photocatalytic

* Corresponding author. Beijing Key Laboratory of Functional Materials for Building Structure and Environment Remediation, School of Environment and Energy Engineering, Beijing University of Civil Engineering and Architecture, Beijing, 100044, China.,

E-mail addresses: chongchenwang@126.com, wangchongchen@bucea.edu.cn (C.-C. Wang).

https://doi.org/10.1016/j.jclepro.2020.123408
0959-6526/

activities can be attributed to the rich active sites (Wang and Wang, 2015), metal-oxide cluster (Wang et al., 2014), tunable pore size and the easily designable physical and chemical functions. For example, Ti-based MOFs NH_2-MIL-125 could reduce Cr(VI) to Cr(III) under visible light irradiation (Wang et al., 2015). Fe-based MOF MIL-88-B(Fe) could efficiently degrade the phenol by photo-Fenton process (Gao et al., 2017). However, pristine MOFs as photocatalysts also suffer from some disadvantages like large band gap (Sun et al., 2014) and quick recombination of photo-induced electrons and holes (Wang et al., 2019a). In order to conquer the above-stated weaknesses and get better photocatalytic performances, it was a feasible strategy to introduce another photocatalyst for modifying the MOFs (Qiu et al., 2018) and building heterostructure (Wang et al., 2019b).

As commonly used photocatalyst, WO_3 demonstrated outstanding photocatalytic performance (Baeck et al., 2003), mainly due to: (i) the narrower band gap ranging from 2.5 to 2.7 eV (Xin et al., 2014), (ii) excellent chemical and thermal stability in aqueous solutions (Liu et al., 2014), (iii) high carrier mobility (Liu et al., 2014), and (iv) facile synthesis methods (Liu et al., 2020). However, the poor reduction ability resulting from the lower conduction band and the fast recombination of photo-gathered carriers may restrict its photocatalytic activity. It was believed that the combination between MOFs and WO_3 may lead to enhanced photocatalytic performance.

Up to now, several cases concerning the WO_3 and MOFs composites were reported to accomplish the organic dyes degradation (Malik and Nath, 2019), pesticide removal (Fakhri and Bagheri, 2020) and H_2S sensing (Zhou et al., 2020). Among the MOFs, Fe-based MOFs was widely used in photocatalytic and photo-Fenton process because of the narrower band gaps, which can be stimulated to produce photo-induced charge carriers under visible light because of the Fe—O clusters (Wang et al., 2018). To our best knowledge, WO_3/MIL-100(Fe) composites haven't been fabricated and used for Cr(VI) reduction and BPA degradation. As well known, ball-milling is a simple and efficient method to accomplish high-throughput production of functional materials or composites with the aid of less solvent or even without any solvent (Chen et al., 2012). It was believed that ball-milling can lead to intimate contacts between the WO_3 and MIL-100(Fe) in molecular scale and facilitate to build heterojunction structure for enhanced photocatalytic activity.

With this paper, WO_3/MIL-100(Fe) composites were fabricated by ball-milling and characterized via different techniques. The WO_3/MIL-100(Fe) composites were adopted to achieve boosted photocatalytic Cr(VI) reduction and photo-Fenton BPA degradation upon the irradiation of visible light (Scheme 1). Also, the possible degradation pathway of BPA decomposition during the photo-Fenton process over M80W120 was clarified. Finally, the corresponding mechanisms of Cr(VI) reduction and BPA degradation over M80W120 were proposed and tested via different techniques.

2. Materials and methods

2.1. Scientific hypothesis

To accomplish the purpose of cleaner production and sustainable development, it was essential to develop new efficient catalysts to achieve photocatalytic Cr(VI) reduction and photo-Fenton organic pollutants (like BPA) degradation under visible light. Two typical catalysts, MIL-100(Fe) and WO_3, were selected to build WO_3/MIL-100(Fe) heterojunction structures with different composition ratios via the green and environment friendly ball-milling method, considering the perfect match of their band gaps, conduction band (CB)/lowest unoccupied molecular orbital (LUMO), and valence band (VB)/highest occupied molecular orbital (HOMO). To affirm the above-stated scientific hypothesis, the photocatalytic Cr(VI) reduction and photo-Fenton BPA decomposition activities over WO_3/MIL-100(Fe) composites were tested, in which the involved mechanisms were proposed and clarified with the aid of different characterization techniques.

2.2. Chemicals

All chemicals are analytical reagent, which were used directly without further purification. Iron(III) chloride hexahydrate ($FeCl_3 \cdot 6H_2O$, 97%), trimesic acid ($C_9H_6O_6$, 99%), bisphenol A ($C_{15}H_{16}O_2$, 96%), and tungsten(VI) oxide nanopowder (WO_3, 99.9%) were purchased from J&K Scientific Company, China. Ethylone glycol ($C_2H_6O_2$, 96%), dimethylformamide (DMF, 99.5%), sodium hydroxide (NaOH), sulfuric acid (H_2SO_4) and potassium dichromate ($K_2Cr_2O_7$, 99%) were supplied by Beijing Chemical Reagent Factory, China. All aqueous solutions were prepared with ultrapure water (18.18 MΩ*cm resistivity at room temperature).

2.3. Experimental procedures

2.3.1. Synthesis of WO_3/MIL-100(Fe) composites

MIL-100(Fe) was fabricated following to the previous literature with slight modification (Xu et al., 2017). Detailly, 51.9 mg $FeCl_3 \cdot 6H_2O$ and 76.6 mg trimesic acid was dissolved in 5 mL ethylone glycol and 5 mL dimethylformamide (DMF), respectively. The matrix was moved into the Teflon-lined autoclave and heated at 393 K for 12 h. The obtained precipitates were centrifuged and washed with deionized water as well as ethanol for 3 times, and finally dried at 333 K for 12 h.

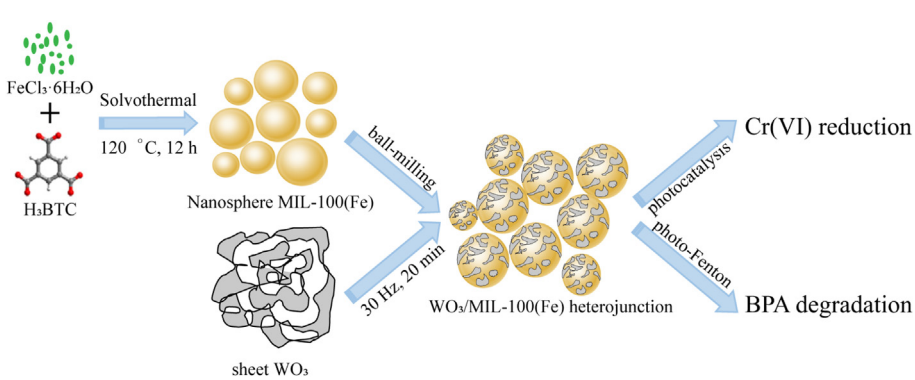

Scheme 1. The flowchart of research methodology in this work.

WO_3/MIL-100(Fe) composites were fabricated by ball-milling. The matrix of MIL-100(Fe) and WO_3 were grinded at 30 Hz for 20 min, which were referred as M*x*W*y* (the letters "M" and "W" represented for MIL-100(Fe) and WO_3, respectively (the "*x*" (120, 100, 80, 60 and 40) and "*y*" (80, 100, 120, 140 and 160) are the mass percentage of MIL-100(Fe) and WO_3).

2.3.2. Characterization methods

The powder X-ray diffraction (PXRD) patterns were obtained on a DX-2700B X-ray diffractometer using Cu Kα radiation. Fourier transform infrared spectra (FTIR) were measured by a Nicolet 6700 infrared spectrophotometer with KBr pellets. X-ray photoelectron spectra (XPS) measurement was performed on a Thermo Escalab Xi^+. The scanning electron microscope (SEM), transmission electron microscopy (TEM) and high-resolution transmission electron microscope (HRTEM) were acquired by SU8020, JEM 1200EX and FEI Talos-S, respectively. UV–vis diffuse reflectance spectra (UV–vis DRS) were tested on a PerkinElmer Lambda 650S spectrophotometer with $BaSO_4$ as the reference with 100% reflectance. Electron spin resonance (ESR) was measured by a JEOL JES-FA200 instrument, in which the 5,5-dimethyl-1-pyrroline-N-oxide (DMPO) was adopted as the spin-trapping agent to detect $\bullet O_2^-$ and •OH radicals.

Electrochemical measurements were analyzed by the Metrohm Autolab PGSTAT204 electrochemical station with 0.2 mol/L Na_2SO_4 aqueous solution (pH = 2.0) as the electrolyte in a typical three-electrode mode. The working electrode was prepared following the following procedure: 5.0 mg MIL-100(Fe), WO_3 or WO_3/MIL-100(Fe) composites were respectively mixed with 260 μL ethanol/Nafion (*v*/*v* = 25/1) under sonication for 30 min. 20.0 μL as-prepared slurry was casted onto the surface of a FTO substrate (1.0 cm × 2.0 cm) as thin film via drop casting method and then dried in air. Finally, the working electrode was successfully fabricated after this process was repeated for several times to obtain smooth and uniform coating. A Pt electrode and a saturated Ag/AgCl electrode were used for the counter electrode and reference electrode, respectively. The transient photocurrent responses and the electrochemical impedance spectroscopy (EIS) measurements were conducted upon the illumination of 300 W Xenon lamp (Beijing Aulight Co., Ltd) as the white light source. The Mott-Schottky determination was carried out in dark, with frequencies of 500, 1000 and 1500 Hz, respectively.

2.3.3. Performance test

All experiments were conducted under the 25 W low power LED light (Beijing Aulight Co., Ltd.), and the light spectrum was depicted in Fig. S1. As to the photocatalytic Cr(VI) reduction, 80.0 mL Cr(VI) solution with the initial concentration being 5 mg/L was treated with 20.0 mg photocatalyst. The suspension was kept stirring in dark for 30 min to reach adsorption-desorption equilibrium. After turning on the light, 2.0 mL suspension was taken out every 20 min and filtered with a 0.22 μm filter to remove photocatalyst from suspension.

The photo-Fenton BPA degradation was conducted under the same light source stated-above, in which 20.0 mg photocatalyst was added to 80.0 mL BPA aqueous solution (10 mg/L). The suspension kept stirring in dark for at least 30 min to reach adsorption-desorption equilibrium. After turning on the light, 15 μL 30% H_2O_2 solution was added to the suspension and 1.5 mL suspension was drawn and filtered with a 0.22 μm filter at specific time interval (first 20 min: every 5 min; after 20 min: every 20 min) to separate photocatalyst from suspension.

2.4. Analysis methods

The Cr(VI) concentration was measured by Auto Analyzer 3 with diphenyl carbazide (DPC) method. A LC20 (Shimadzu) system was used to determine the concentration of residual BPA after the photo-Fenton degradation. The experimental sample were separated on a C18 column (5.0 μm, 2.1 mm × 250 mm). LC determination method of BPA was listed as the following: acetonitrile and were used as mobile phases A and B, and the ratio of A/B is 55/45. The detector was set at the wavelength of 227 nm. The BPA degradation products were analyzed by a LC-MS system (Agilent 1100LC/MS Trap SL).

3. Results and discussion

3.1. Characterizations

The PXRD patterns of M*x*W*y* composites, individual MIL-100(Fe) and WO_3 were displayed in Fig. 1a. The characteristic PXRD peaks of MIL-100(Fe) matched perfectly with those in previous reference (Xu et al., 2017). As well, the PXRD patterns of WO_3 matched perfectly with the standard one (JCPDS No. 97-008-0057), in which the peaks at 23.1°, 23.6°, 24.4°, 33.3°, 34.1°, 34.2° and 49.9° corresponded to (0 0 2), (0 2 0), (2 0 0), (0 2 2), (2 0 2), (2 2 0) and (4 0 0) planes of WO_3, respectively. All the characteristic diffraction peaks of composites matched well with pristine WO_3. No obvious characteristic diffraction peaks of pure MIL-100(Fe) could be observed mainly due to the mask of WO_3 and relatively low diffraction intensity (Liang et al., 2015b).

The successful fabrication of M*x*W*y* was verified by the FTIR spectra result. As displayed in Fig. 1b, the strong signal at 711 cm^{-1} is the characteristic peak of benzene ring in trimesic acid. The peaks observed at 1615, 1575, 1451, and 1385 cm^{-1} can be assigned to the carboxyl groups (Song et al., 2014). And, the peaks at the range of 450–900 cm^{-1} were identified as the stretching vibration of W–O–W (Fu et al., 2019). With the increasing mass percentage of MIL-100(Fe), the benzene ring peaks ranging from 700 to 800 cm^{-1} could be observed more clearly (Abdpour et al., 2018).

XPS determination was carried out to figure out the chemical interactions between MIL-100(Fe) and WO_3 (Fig. 2a). M80W120 was selected to compare with pure WO_3 and MIL-100(Fe). Two obvious W 4f and Fe 2p peaks could be identified as the WO_3 and MIL-100(Fe). The peaks located at 711.36 eV and 724.73 eV could be assigned to the Fe $2p_{3/2}$ and Fe $2p_{1/2}$ (Fig. 2b) (Castro et al., 2012). After ball-milling, it was obvious to find that the Fe $2p_{3/2}$ and Fe $2p_{1/2}$ peaks were shifted to 711.05 eV and 724.46 eV in M80W120, respectively. The shift of Fe 2p peaks towards the lower binding energy implied that the electrons might be transferred from WO_3 to MIL-100(Fe) (Yu et al., 2015). Moreover, the HRTEM images can also investigate the interaction between MIL-100(Fe) and WO_3. As shown in Fig. 3e and f, the MIL-100(Fe) were wrapped by the WO_3 nano-sheets, in which new interfaces were formed between MIL-100(Fe) and WO_3.

The micromorphology and microstructure of MIL-100(Fe), WO_3 and their composites were observed by TEM and SEM images (Theingi et al., 2019). As displayed in Fig. 3 and Fig. S2, the pure MIL-100(Fe) displayed nanospheres with the diameters ranging from 200 to 400 nm (Xu et al., 2017). The pristine WO_3 is presented as small nanosheets with the size in the range of 30–60 nm, which could be easily distinguished from MIL-100(Fe) (Wang et al., 2009). After ball milling, it can be observed that the MIL-100(Fe) spheres were wrapped by WO_3 nanosheets, in which the structure and shape of MIL-100(Fe) were slightly changed. The HRTEM image of M80W120 (Fig. 3e and f) revealed that the lattice spacings of 0.39 nm and 0.37 nm could be assigned to the (001) and (002)

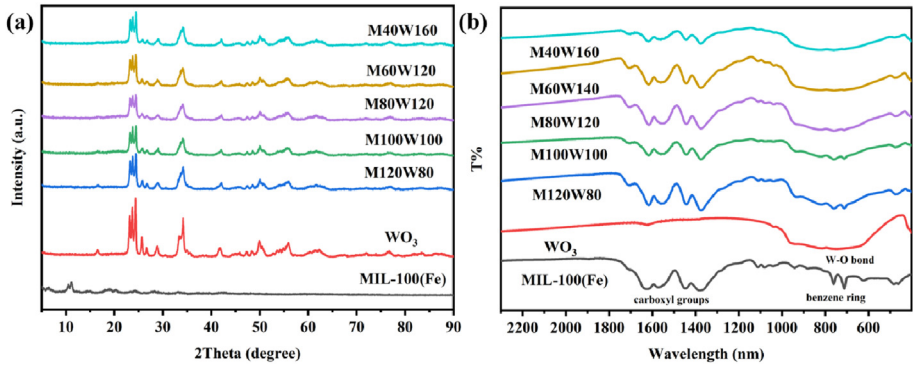

Fig. 1. (a) The PXRD patterns and (b) the FTIR spectra of the M*x*W*y* composites, WO_3, and MIL-100(Fe).

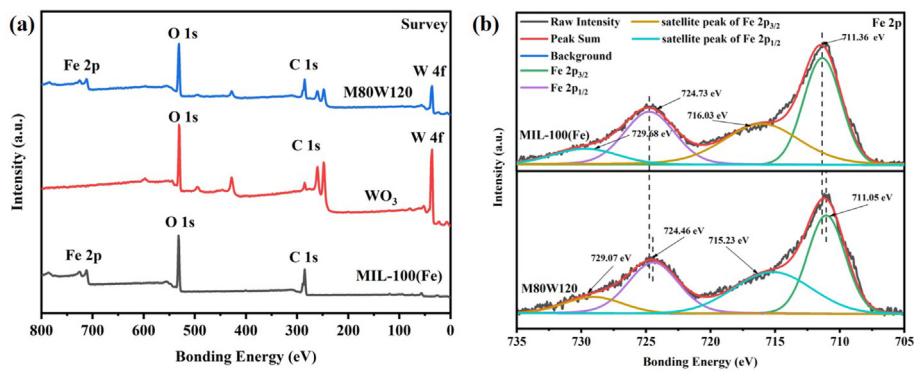

Fig. 2. The XPS spectra of M80W120, WO_3 and MIL-100(Fe): (a) survey scan, (b) Fe 2p.

facets of WO_3, further indicating the successful modification between MIL-100(Fe) and WO_3 (Zhang et al., 2018). The elemental analysis affirmed the distribution of WO_3 and MIL-100(Fe) throughout M80W120 (Fig. 4). All the characterizations confirmed the successful fabrication of the composites by ball milling.

The UV–visible DRS and E_g plots of M*x*W*y* composites, WO_3 and MIL-100(Fe) were demonstrated in Fig. 5a and b. The absorption edges of individual WO_3 and MIL-100(Fe) at about 500 nm and 650 nm corresponded to the band gaps of 2.51 eV (Ahmad et al., 2019) and 2.76 eV (Liu et al., 2020), respectively. The light absorption regions of M*x*W*y* composites are almost consistent with that of MIL-100(Fe), and their E_g values are in the range of 2.5–2.75 eV, indicating that all the M*x*W*y* composites might display their photocatalytic activities under visible light.

The flat band potentials of the pristine WO_3 and MIL-100(Fe) could be determined from the Mott-Schottky plots. As shown in Fig. 5c and d, the positive correlations between the potential and the C^{-2} of both MIL-100(Fe) and WO_3 indicated that they are all typical *n*-type photocatalysts (The flat band potential equals the CB potential) (Liang et al., 2015b; Lima et al., 2015). So, the flat band potential of the WO_3 and MIL-100(Fe) were identified to be −0.18 eV and −0.63 eV, respectively.

3.2. Photocatalytic activity

3.2.1. Photocatalytic Cr(VI) sequestration

As depicted in Fig. 6a, there is no obvious adsorption between WO_3/MIL-100(Fe) and Cr(VI) during the adsorption-desorption process in dark. According to the previous work, the zeta potential of MIL-100(Fe) and WO_3 are negative valve at pH = 2 (MIL-100(Fe): about -5mV (Huo and Yan, 2012), WO_3: about −20mV (Su et al., 2017)). At pH = 2, the dominating form of Cr(VI) is $Cr_2O_7^{2-}$ or $HCrO_4^-$ (Zhao et al., 2019), implying that no electrostatic adsorption interaction between WO_3/MIL-100(Fe) and Cr(VI). Moreover, MIL-100(Fe) was wrapped by WO_3 nanosheets, WO_3 displayed no obvious adsorption performance due to its structure characteristics.

Under the irradiation of visible light, both pristine MIL-100(Fe) and WO_3 showed negligible Cr(VI) reduction activities. While, all M*x*W*y* composites accomplished higher photocatalytic activities under visible irradiation than the pristine MIL-100(Fe) and WO_3. Among the M*x*W*y* composites, M80W120 composite displayed highest photocatalytic performance, which can achieve 100% Cr(VI) reduction within 60 min (Fig. 6a). The kinetic plots of Cr(VI) removal were fitted to the pseudo-first order model (Li et al., 2019). The Cr(VI) removal rates (*k* values) can further indicate that M80W120 exhibited best photocatalytic ability. Comparing with other photocatalysts, M80W120 composite also exhibited superior photocatalytic activity toward Cr(VI) reduction under identical reaction conditions (Table 1).

3.2.1.1. Influence of initial pH. It is widely accepted that the pH values of solution have strong influence on photocatalytic activities, since it can affect both acid-base environment and presence states of Cr(VI) (Du et al., 2019). The influences of different initial pH towards Cr(VI) were illustrated in Fig. 6c. Obviously, the removal efficiency decreased sharply with the rising pH, in which the highest reduction efficiency (100% within 60 min) was accomplished at pH = 2.0. The Cr(VI) sequestration mainly followed Eqs. (1)–(3) in acidic conditions (Chen et al., 2020). In alkaline solution, the reaction mainly follows Eqs. (1) and (4), in which the $Cr(OH)_3$ precipitates will be deposited on the surface of material under high pH

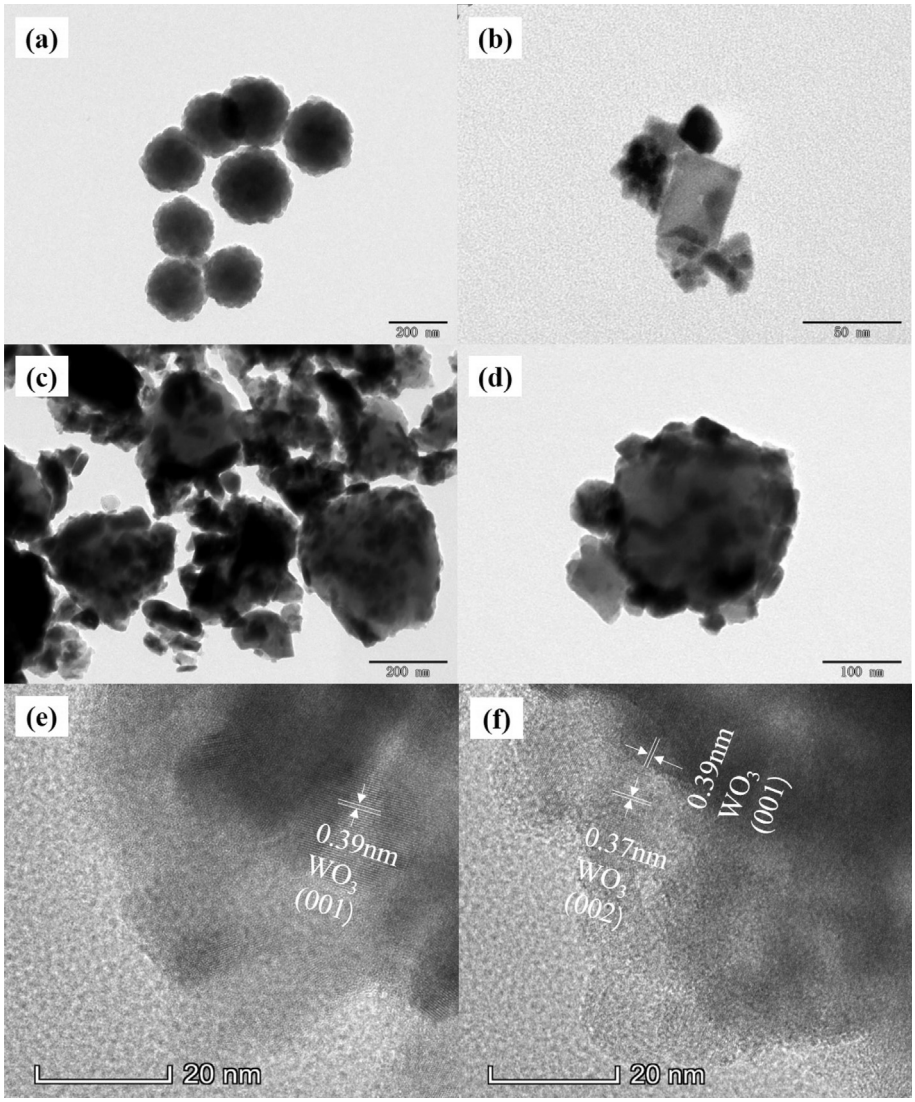

Fig. 3. The TEM images of (a) MIL-100(Fe), (b) WO_3, (c) and (d) M80W120, (e) and (f) HRTEM of M80W120.

value, leading to the inhibited Cr(VI) removal efficiency (Zhou et al., 2019).

$$M80W120 + h\nu \rightarrow M80W120\ (h^+ + e^-) \quad (1)$$

$$Cr_2O_7^{2-} + 14H^+ + 6e^- \rightarrow 2Cr^{3+} + 7H_2O \quad (2)$$

$$HCr_2O_7^- + 7H^+ + 3e^- \rightarrow Cr^{3+} + 4H_2O \quad (3)$$

$$CrO_4^{2-} + 4H_2O + 3e^- \rightarrow Cr(OH)_3 + 5OH^- \quad (4)$$

3.2.1.2. Influence of low weight organic molecules. Under the visible irradiation, M80W120 could be excited to create photo-gathered electrons and holes, electrons had reducing power, which could transfer Cr(VI) to Cr(III). To explore the influence of low weight organic molecules as hole scavengers in Cr(VI) removal, three organic acids were added to capture holes in experiment. As shown in Fig. 6d, the organic acids enhanced the Cr(VI) removal efficiency, because the holes (h^+) was consumed by the organic molecules and more electrons were left to transfer Cr(VI) to Cr (III) (Barrera-Diaz et al., 2012).

3.2.1.3. Influence of foreign ions. To study the effect of co-existing foreign ions on the photocatalytic activities, lake water (from Ming Lake in Daxing campus, BUCEA), tap water (Daxing campus, BUCEA), simulated sea water and simulated leather wastewater (the detailed information can be found in Table S1 of ESI) were adopted to formulate Cr(VI) solutions, which were further used to carry out the photocatalytic experiments over M80W120 upon the visible light illumination. As exhibited in Fig. 6e, the removal efficiency decreased in the tap water and simulated sea water (Wang et al., 2012) because of the inhibition of co-existing inorganic ions like NO_3^-, Cl^- and SO_4^{2-} (Vignesh et al., 2013). While, the Cr(VI) reduction reaction rate became faster in the lake water, which might be attributed to the consumption of hole (h^+) by the dissolved organic matters (DOM) in lake water (Zhao et al., 2019). In Fig. 6e (inset), the reaction rate decreased heavily in simulated leather tanning water, it may be due to the high contents of initial Cr(VI) and foreign inorganic ions (Yi et al., 2019).

3.2.1.4. Reusability and stability of M80W120. To test the reusability of M80W120, the photocatalytic cycling experiment was conducted

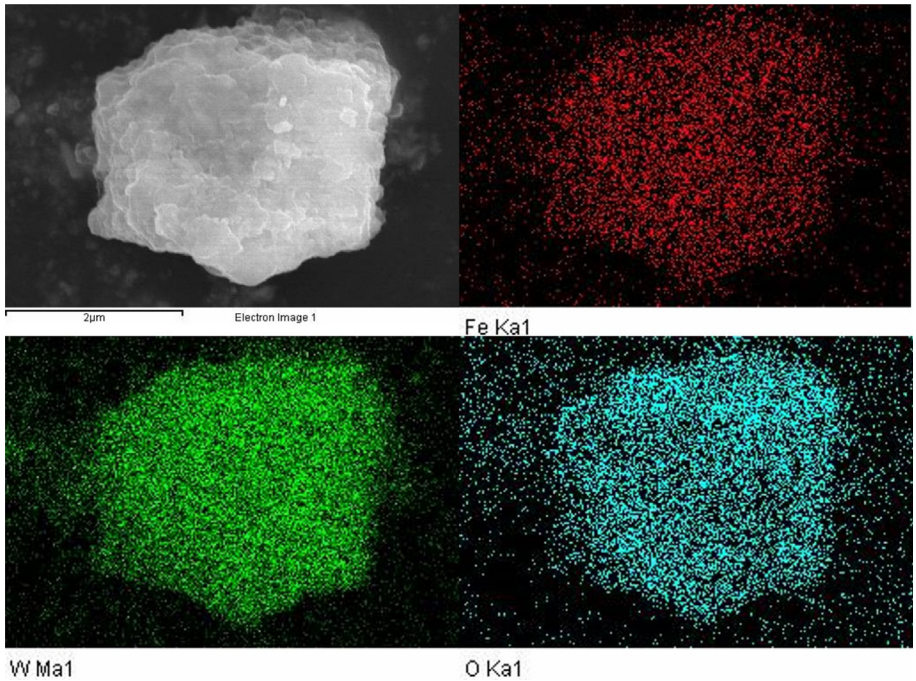

Fig. 4. The scan mapping elemental analysis of M80W120 composite.

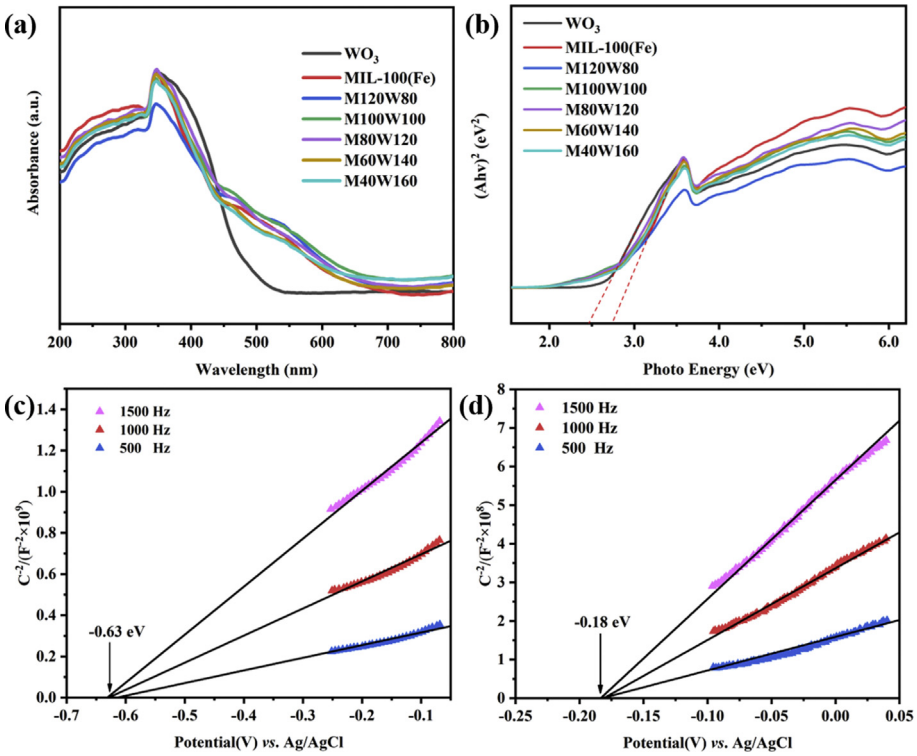

Fig. 5. The UV–vis DRS (a) and E_g plots (b) of the MIL-100(Fe), WO_3 and series composites. Mott-Schottky plots of (c) MIL-100(Fe) and (d) WO_3 at different frequencies.

with M80W120 upon the visible light illumination (Awual et al., 2019). As depicted in Fig. 7a, no noticeable Cr(VI) reduction efficiency decline was observed over M80W120 during the five cycles experiments, which still can achieve 100% Cr(VI) reduction in 80 min. As well, the PXRD patterns (Fig. 7b) of M80W120 after 5 runs experiments matched well with those of fresh samples, which could further confirm that M80W120 was highly stable and efficient during long-term photocatalytic operation.

3.2.2. Photo-Fenton degradation of bisphenol A (BPA)

To evaluate the photo-Fenton oxidation performance of M80W120, series blank experiments as control tests were

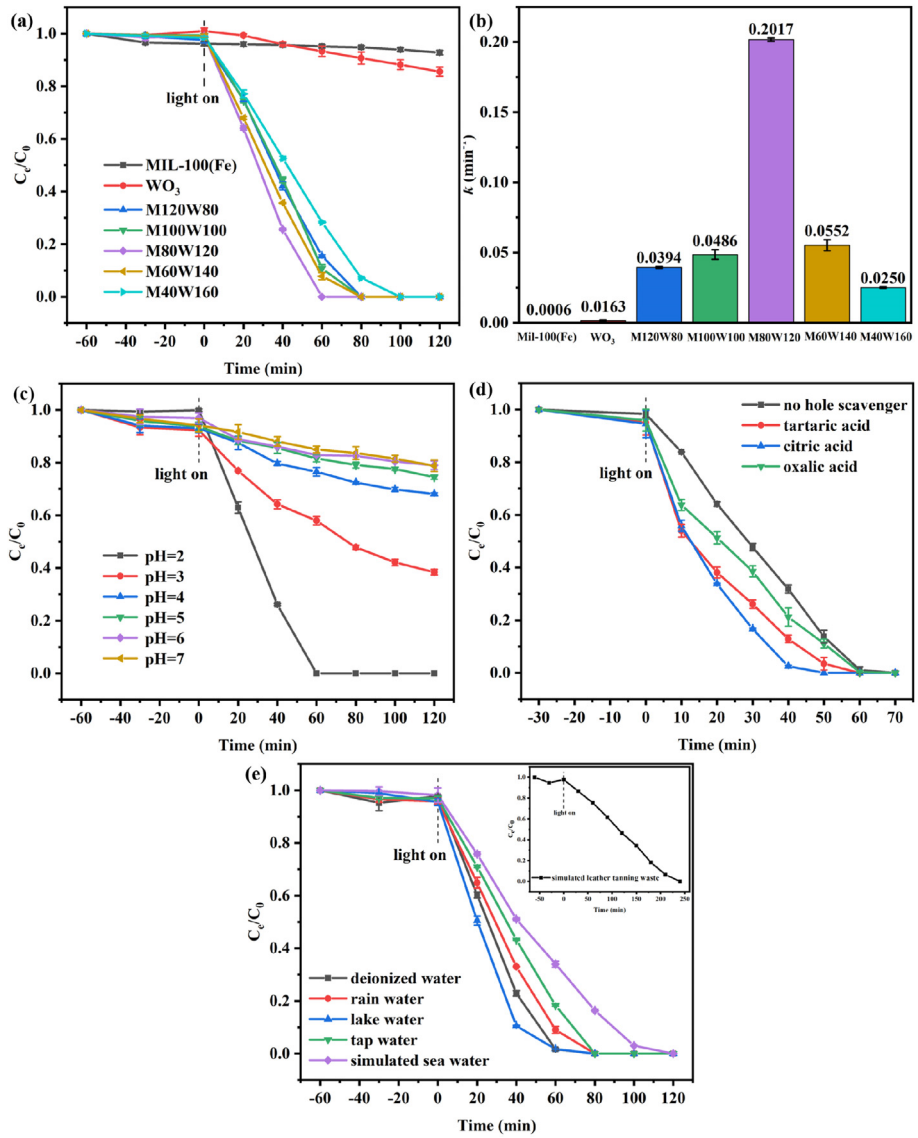

Fig. 6. (a) Photocatalytic Cr(VI) sequestration efficiencies and (b) the reaction rate constants (k) of different photocatalysts. (c) The effect of initial pH; (d) the effect of small organic acids; (e) the effect of foreign ions on the reduction of Cr(VI).

Table 1
Comparison of Cr(VI) reduction performance of some representative photocatalysts.

Photocatalyst/Amount (mg)	V (mL)/C_0 (mg/L)/pH	Light source	Time/(min)	Efficiency (%)/cycles	Ref.
Fe@WO_3/-	100/10/-	300 W Xe lamp	120	95/5	Feng et al. (2019)
g-C_3N_4/MIL-53(Fe)/20	50/10/2.0–3.0	500W Xe lamp	180	99/4	Huang et al. (2017)
g-C_3N_4/NH_2-MIL-101(Fe)/20	40/10/2.0	300 W Xe lamp	60	100/3	Liu et al. (2018)
g-C_3N_4/MIL-100(Fe)/100	200/10/2.0	300 W Xe lamp	80	97/5	Du et al. (2019)
WO_3/MIL-53(Fe)/200	100//10/2.5	sunlight	240	94/4	Oladipo (2018)
WO_3/MIL-100(Fe)/20	80/5/2.0	25W LED light	60	100/5	This work

conducted to study the BPA oxidative decomposition efficiencies in different processes. As illustrated in Fig. 8a, pure WO_3 and H_2O_2 had little effects on BPA oxidation and the degradation efficiency of pure M80W120 could reach 22.3%. After adding H_2O_2, the oxidative decomposition efficiency of BPA with MIL-100(Fe) and M80W120 was notably enhanced, which could complete degrade the BPA within 20 min (M80W120) and 40 min (MIL-100(Fe)). While in the dark, there was no obvious decline of BPA with the combination of M80W120 and H_2O_2. It could be concluded that photo-Fenton played a dominant role in BPA degradation. The kinetic plots of BPA decomposition were fitted perfectly with the pseudo-first order model. As well, the photocatalytic BPA degradation rates (k values) (Fig. 8b) can further confirm the dominant role of photo-Fenton process. Additionally, the photocatalytic performance of BPA degradation among M80W120 and the other photocatalysts was also compared in Table 2. The results indicated that M80W120 exhibited superior photo-Fenton degradation activity toward bisphenol A.

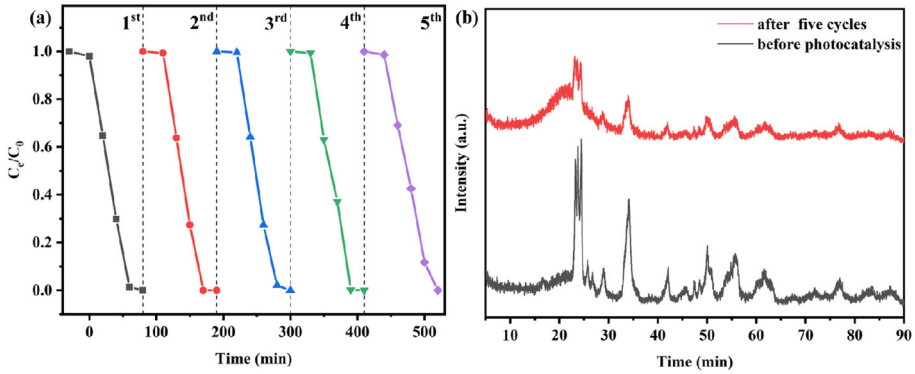

Fig. 7. (a) The cycle experiment of Cr(VI) sequestration with M80W120; (b) PXRD patterns of fresh and used M80W120 samples.

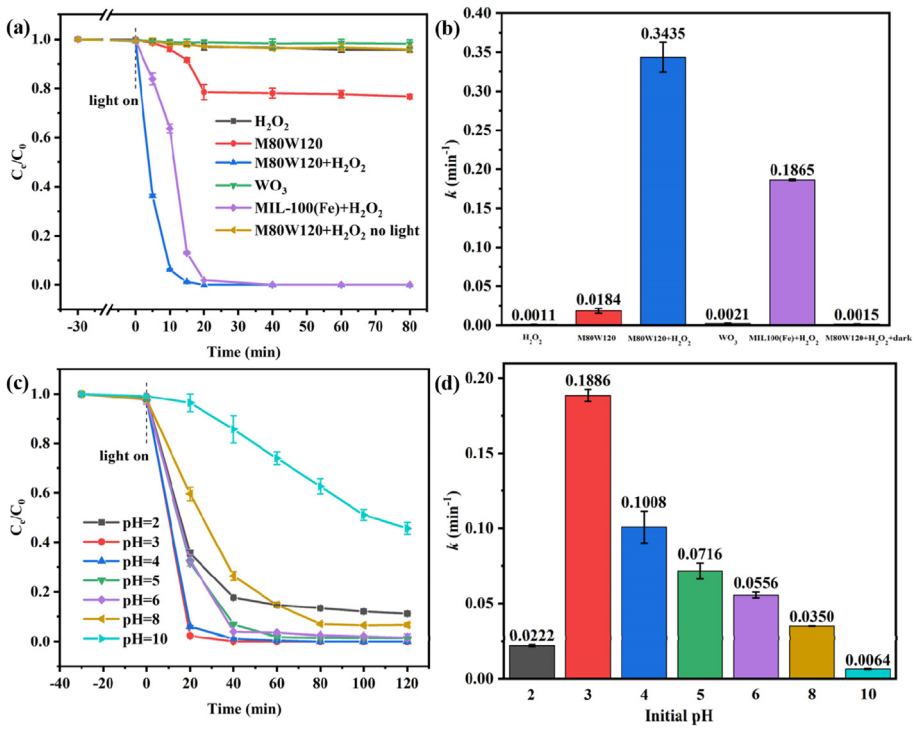

Fig. 8. (a) Photocatalytic BPA degradation efficiencies and (b) the reaction rate (k) of experiments of different photocatalysts. (c) The effects of initial pH on BPA degradation. (d) The photocatalytic BPA degradation rates (k values) under the different initial pH.

Table 2
Comparison of BPA degradation performance of some representative photocatalysts.

Photocatalyst/Amount (mg)	V (mL)/C_0 (mg/L)/pH	Light source	Time/(min)	Efficiency(%)/cycles	Ref.
WO_3/TiO_2/12.5	200/10/-	150 W Hg lamp	120	100/-	Žerjav et al. (2017)
Ag/AgCl/Fh/H_2O_2/50	50/30/3.0	5 W LED light	60	100/4	Zhu et al. (2018)
g-C_3N_4/MIL-101(Fe)/PS/-	-/10/-	300 W Xe lamp	60	98/5	Gong et al. (2018)
ZnO/MIL-100(Fe)/H_2O_2/10	50/5/2.0	500 W Xe lamp	120	95/5	Ahmad et al. (2019)
Pd@MIL-100(Fe)/H_2O_2/5	40/20/4.0	300 W Xe lamp	150	99.5/4	Liang et al. (2015b)
WO_3/MIL-100(Fe)/H_2O_2/20	80/10/3.0	25W LED light	20	100/5	This work

3.2.2.1. Effect of pH toward BPA degradation. The initial pH of the solution can make great difference on the photo-Fenton process (Cheng et al., 2018). As illustrated in Fig. 8c, the BPA oxidation efficiency of M80W120 was highest at pH = 3.0 and decreased with the elevated pH. It was found that M80W120 can display good BPA degradation activities with efficiencies from 100% to 90% within 40 min in wide pH range of 3.0–6.0. While, the further increase of pH led to sharp decrease of BPA decomposition efficiency, in which the BPA could not be degraded completely in 120 min. It was deemed that H_2O_2 tends to be decomposed into molecular oxygen and H_2O in alkaline environment (Zhang et al., 2009). As well, M80W120 performed worse at pH = 2, due to that the formation of $H_3O_2^+$ could inhibit the formation of •OH radicals under strong acid condition like pH < 3.0 (Chen et al., 2009). The photo-Fenton BPA

degradation rates (k values) (Fig. 8d) could further affirmed that M80W120 performed best degradation efficiency and rate at pH = 3.0.

3.2.2.2. Effect of H_2O_2 dosage toward BPA degradation. The influence of H_2O_2 amount on BPA oxidation was shown in Fig. 9a. When the dosage of H_2O_2 increased from 37.50 μL/L to 56.25 μL/L, the degradation efficiency increased from 90% to 100%. The enhanced oxidation efficiency can be contributed to the increase amount of •OH radicals with increasing dosage of H_2O_2 (Ai et al., 2014). However, when the dosage increased from 56.25 μL/L to 112.50 μL/L, the degradation efficiency was not further enhanced and the degradation rate became slower, which might be resulted from the capture of •OH by surplus H_2O_2 to form less reactive species (Eq. (5)) to inhibit the BPA degradation (Xu and Wang, 2011).

$$H_2O_2 + \bullet OH \rightarrow HOO\bullet + H_2O_2 \rightarrow H_2O + O_2 \quad (5)$$

3.2.2.3. Reusability and stability of M80W120 toward BPA degradation. The reusability and stability of catalysts are key issues to be considered (Teo et al., 2019). As shown in Fig. 9b, the BPA degradation over M80W120 exhibited no obvious decline after 5 cycles, indicating that M80120 is stable and can be recycled for BPA degradation. The PXRD (Fig. 9c) and TEM image (Fig. 9d) of used M80W120 matched well with fresh samples, which could further confirm the stability and reusability of M80W120. As illustrated in Fig. S3, the concentration of leached Fe ions after each cycle was around 1.9 mg/L, which was conform to the environmental standards (2 mg/L) set by the European Union (Gao et al., 2017).

3.2.2.4. Pathway of BPA degradation. As illustrated in Fig. 10, BPA was firstly attacked by •OH radicals to form hydroxylated BPA (m/z = 261) (Meng et al., 2019). Then, the fracture of the isopropyl group resulted in the formation of phenol (PhO) radicals and isopropylphenol (IPP) radicals (Molkenthin et al., 2013). The PhO radical may form hydroxylated intermediates and further lead to the formation of hydroquinone and phenol, while IPP radical was converted to 4-isopropenylphenol and then further formed to 4-hydroxy-acetophenone and 4-isopropylenecatechol (Lin et al., 2020). Eventually, lower molecular weight products were produced mainly due to the further attack of hydroxyl radicals (Sharma et al., 2015).

3.2.3. Possible mechanisms

The photoluminescence (PL) spectra of M80W120, MIL-100(Fe) and WO_3 obtained from Techcomp FL970 fluorescence spectrometer were used to judge the separation efficiency of photo-induced charge carriers. It was deemed that lower PL intensity means faster separation efficiency of the photo-generated holes and electrons (Chen et al., 2014). MIL-100(Fe), WO_3, and their composites were excited at 345 nm to yield the emission peaks centered at 450 nm. As shown in Fig. 11, the PL intensity of M80W120 was lower than other photocatalysts, indicating that M80W120 demonstrated boosted separation of photo-generated charge carriers. Moreover, photo-induced electrons and holes separation efficiency could be further confirmed by photocurrent determination and electrochemical impedance spectroscopy (EIS). It can be seen that M80W120 accomplished higher photocurrent response than that of MIL-100(Fe), WO_3 and other composites, suggesting that the composites between MIL-100(Fe) and WO_3 could weaken the recombination between holes and electrons (Zhang et al., 2017). Moreover, the Nyquist arc radius (Fig. 11c) of M80W120 was smaller than those of WO_3, MIL-100(Fe) and other composites, implying that the composites possessed smaller charge transfer

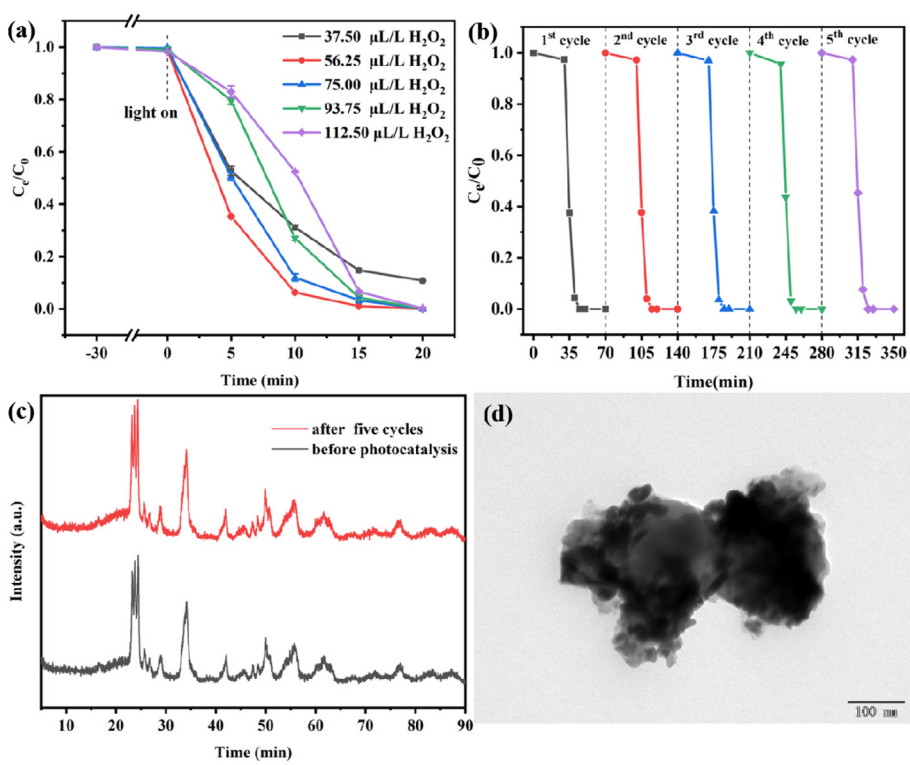

Fig. 9. (a) The effects of H_2O_2 dosage on BPA degradation under pH = 3.0. (b) The cycle experiments of photocatalytic BPA degradation over M80W120; (c) PXRD patterns of M80W120 before and after cycle experiment; (d) TEM images of M80W120 after cycle experiments.

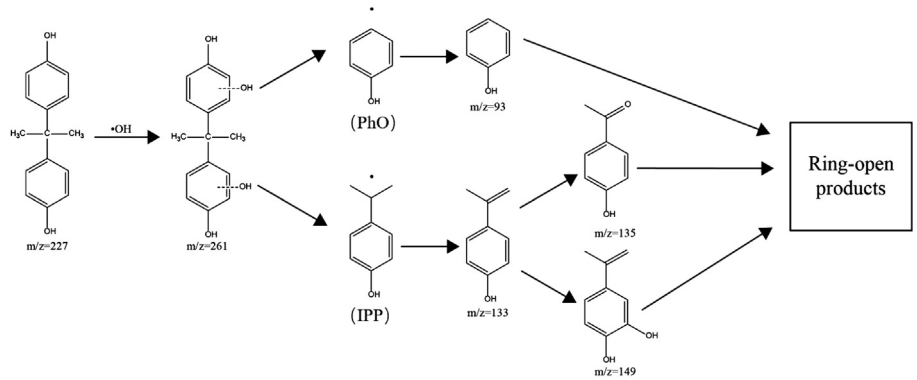

Fig. 10. The pathway for BPA decomposition in M80W120/Vis/H_2O_2 system.

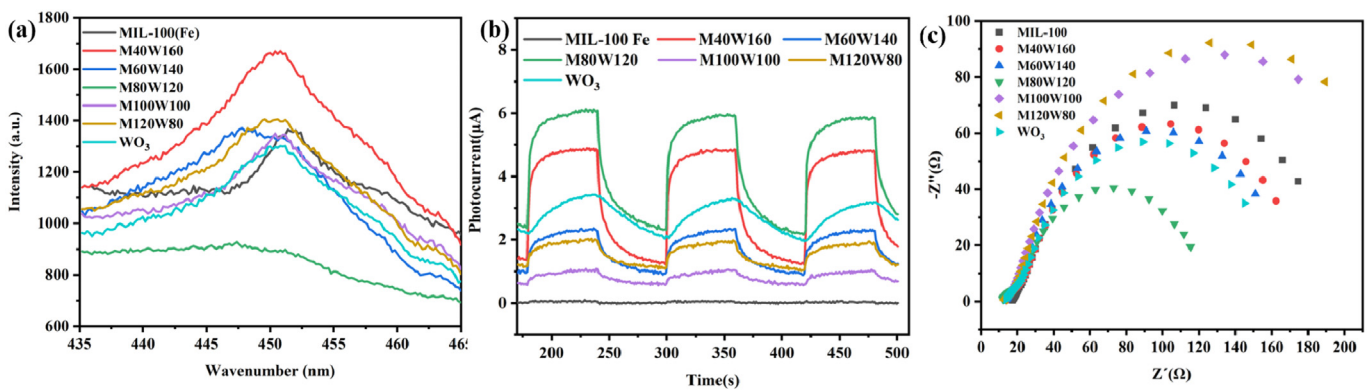

Fig. 11. (a) The PL spectra, (b) photocurrent response density, (c) EIS analysis of MIL-100(Fe), WO_3 and their composites.

resistance (Niu et al., 2018).

To further study the photocatalytic reaction mechanism, series capture experiments were designed to figure out the active species produced by M80W120, in which the EDTA-2Na, *p*-benzoquinone (BQ), isopropyl alcohol (or *t*-butanol) (IPA) and $AgNO_3$ were used as scavengers to capture h^+, $\bullet O_2^-$, •OH radicals and e^- (Zhao et al., 2019), respectively. Nitrogen gas was purged into reaction system to remove dissolved O_2 (DO) to further avoid the formation of $\bullet O_2^-$ (Wang et al., 2016). As depicted in Fig. 12a, the Cr(VI) reduction efficiency declined significantly with the addition of $AgNO_3$, indicating that the electrons played dominant role in Cr(VI) reduction (Shi et al., 2015). The introduction of EDTA-2Na enhanced the Cr(VI) removal notably, implying that the enhanced separation of holes and electrons resulting from the quick consume of holes led to more electrons for Cr(VI) being reduced into Cr(III) (Zhou et al., 2019). A moderate decline was observed in N_2 atmosphere, indicating that $\bullet O_2^-$ also played the role of Cr (VI) removal (Zhou et al., 2019). In the addition of IPA, a small drop occurred in Cr(VI) reduction, which could be due to the equilibrium moving toward Cr(VI) (Eq. (7)) (Yi et al., 2019).

$$H_2O_2 + Cr(III) + H^+ \rightarrow Cr(VI) + H_2O + \bullet OH \quad (6)$$

During the BPA degradation, •OH radicals were considered as the critical specie in Fenton process (Tang and Wang, 2019). As demonstrated in Fig. 12b, the BPA degradation decreased obviously with the addition of TBA, implying that •OH played dominant role in the degradation of BPA. The addition of BQ exerted no noticeable inhabitation to BPA degradation, implying that $\bullet O_2^-$ displayed no influence on BPA degradation (Guo et al., 2019). It was worthy to noting that EDTA-2Na induced negative effect on BPA degradation, due to the equilibrium between h^+ and •OH following by Eq. (7) (Yi et al., 2019).

$$2H_2O + h^+ \rightarrow 2\bullet OH + H^+ \quad (7)$$

As well, the terephthalic acid (TA) fluorescence was achieved on Techcomp FL970 fluorescence spectrometer to detect •OH to further confirm its influence in photo-Fenton BPA oxidation. As shown in Fig. 12c and d, the addition of H_2O_2 resulted into observed increase fluorescence intensity, more •OH radicals were gathered in photo-Fenton system (Ye et al., 2018). It was confirmed that •OH radicals produced in photo-Fenton process were the critical active specie to control the BPA oxidation (Jiang et al., 2018).

The electron spin-resonance spectroscopy (ESR) analysis was also conducted to determine the active species in experiments. As shown in Fig. 12e and f, no signal could be observed in dark. And the •OH and $\bullet O_2^-$ intensities in 10 min were stronger than those in 5 min, suggesting that both •OH and $\bullet O_2^-$ were generated upon the illumination of visible light. It was noteworthy noting that $\bullet O_2^-$ could be produced over MIL-100(Fe), while a weak signal $\bullet O_2^-$ could be observed over pure WO_3 after 10 min illumination. The •OH radicals could be produced by pure WO_3 under the irradiation of visible light, in which the faint signals could be observed over MIL-100(Fe) after 10 min illumination (Fig. S4). Considering that the position of HOMO of MIL-100(Fe) (2.33 eV *vs* NHE) was higher than the standard potential of the OH^-/•OH pair (2.40 eV *vs* NHE), and the position of the valence band of WO_3 (2.53 eV vs NHE) was lower than the standard potential of OH^-/•OH, it can be concluded that the photo-generated holes over WO_3 rather than MIL-100(Fe) could

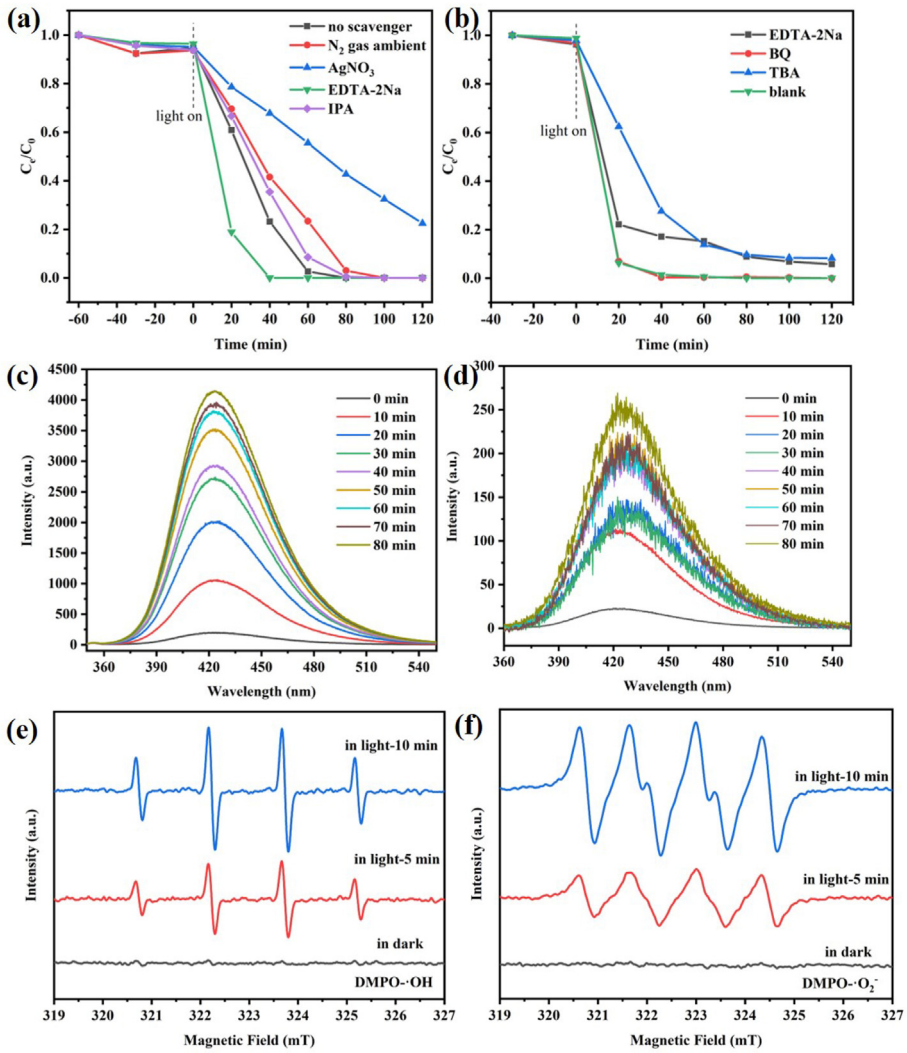

Fig. 12. Capture experiment of Cr(VI) reduction (a) and photo-Fenton BPA degradation (b) over M80W120. Fluorescence spectral changes with the presence of H_2O_2 (c); with the absence of H_2O_2 (d); ESR spectra of (e) •OH and (f) $•O_2^-$ radicals for M80W120.

react with OH^- or H_2O to form •OH. In addition, the position of LUMO of MIL-100(Fe) (−0.43 eV *vs* NHE) was higher than the standard potential of the $O_2/•O_2^-$ pair (−0.33 eV *vs* NHE) and the position of the conduction band of WO_3 (0.02 eV vs NHE) was lower than the standard potential of $O_2/•O_2^-$, the $•O_2^-$ radicals could be produced by MIL-100(Fe) instead of WO_3 (Zhou et al., 2019). Moreover, the signals of •OH and $•O_2^-$ were stronger over M80W120 than those of pure MIL-100(Fe) and WO_3, implying that M80W120 can yield more radicals to accomplish the enhanced photocatalytic ability.

The possible Z-scheme mechanism for photo-Fenton BPA decomposition and photocatalytic Cr(VI) removal over M80W120 was proposed and exhibited in Fig. 13a. Under visible light, both MIL-100(Fe) and WO_3 could be excited to yield photo-generated holes and electrons. The excited electrons on the CB of WO_3 were more easy to be transferred to the HOMO of MIL-100(Fe) to combine with holes, in which the charge transmission promoted the separation of electron-hole pairs and allowed the electrons and holes to remain on the LUMO of MIL-100(Fe) and VB of WO_3, respectively. Since the position of LUMO of MIL-100(Fe) (−0.43 eV vs NHE) was much higher than the redox potential of Cr(VI)/Cr(III) (1.05 eV vs NHE, pH = 2.0), the electrons on the LUMO of MIL-100(Fe) could easily reduce the Cr(VI) in to Cr (III) (Yi et al., 2019). Considering that the redox potential of $O_2/•O_2^-$ at −0.33 eV was lower than LUMO of MIL-100(Fe), $•O_2^-$ could be produced by the dissolved O_2 and electrons, and participate into the Cr(VI) removal (Zhou et al., 2019).

On the other hand, the efficient BPA degradation was mainly resulted from the Fenton-like transformation between Fe(III) species and Fe(II) species (Eq. (8) and (9)) (Cheng et al., 2018), which could produce •OH to oxidize BPA (Lv et al., 2015). Furthermore, the electrons over the LUMO of MIL-100(Fe) and the holes over the VB of WO_3 could also participate in the BPA degradation following Eq. (7)- (10), respectively (Ai et al., 2014). The proposed Z-scheme can be affirmed by both the active species capture and the ESR analysis.

$$\text{Fe(III) species} + H_2O_2 \rightarrow \text{Fe(II) species} + HO_2• + H^+ \quad (8)$$

$$\text{Fe(II) species} + H_2O_2 \rightarrow \text{Fe(III) species} + •OH + OH^- \quad (9)$$

$$H_2O_2 + e^- \rightarrow •OH + OH^- \quad (10)$$

The photo-deposition of Pt and PbO_2 nanoparticles were conducted over M80W120 to further confirm the charge transfer route.

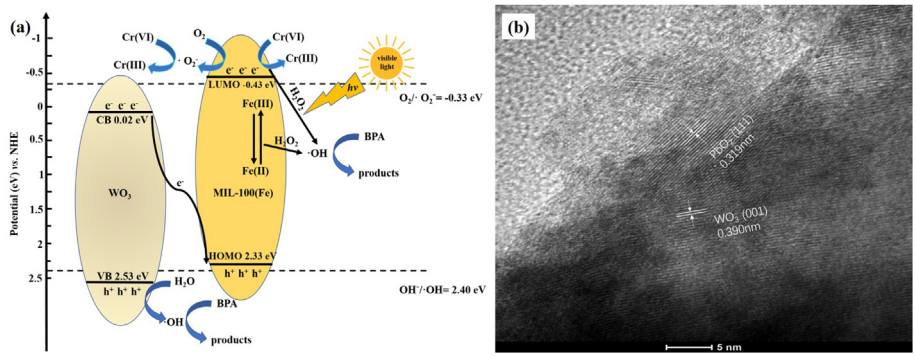

Fig. 13. (a) The diagram of photocatalytic Cr(VI) sequestration and photo-Fenton BPA decomposition mechanism of M80W120. (b) HRTEM images of photo-deposited PbO_2 over M80W120.

It was deemed that Pt nanoparticles could be formed by the reduction of H_2PtCl_6 by accepting the electron and PbO_2 nanoparticles could be yielded by the oxidation of Pb^{2+} with the aid of the hole, in which Pt and PbO_2 would be deposited on the sites of photo-generated electron and hole flow, respectively (Jiang et al., 2019). If the M80W120 system followed the Z-scheme, Pt and PbO_2 nanoparticles would be deposited around the MIL-100(Fe) nanospheres and WO_3 nanosheets, respectively. In Fig. 13b, the lattice fringes of 0.390 and 0.319 nm could be assigned to the (001) facet of WO_3 and (111) facet of PbO_2, implying that the photo-generated holes left over the WO_3 led to the formation of PbO_2 nanoparticles from Pb^{2+} (Jiang et al., 2018). However, it was hard to observe the deposited Pt NPs over MIL-100(Fe) from HRTEM image, probably due to that MIL-100(Fe) spheres were completely wrapped by WO_3 nanosheets. The photo-deposition of Pt and PbO_2 NPs over M80W120 can provide another solid proof to confirm the formed Z-scheme photocatalytic system.

4. Conclusion

Series WO_3/MIL-100(Fe) composites were successfully fabricated by ball-milling. Comparing with other photocatalysts, the optimal M80W120 composite showed outstanding photocatalytic Cr(VI) reduction performance and photo-Fenton BPA decomposition activity upon the irradiation of visible light, which resulted from the construction of Z-scheme between the MIL-100(Fe) and WO_3. Electrochemical, ESR analysis along with the photo-deposition of Pt and PbO_2 confirmed the fabrication of Z-scheme heterojunction. During the photoreduction of Cr(VI) into Cr(III) and the photo-Fenton BPA degradation, the influence of initial pH, foreign ions, low-weight organic molecules and H_2O_2 dosage on photocatalytic performance were also clarified. In addition, the cycle experiment of Cr(VI) reduction and BPA degradation revealed that M80W120 composite was stable and recyclable, the composite could maintain the photocatalytic activities for more than 5 successful cycles. As well, the BPA degradation pathway during the photo-Fenton like treatment were proposed and tested. The WO_3/MIL-100(Fe) composites have huge application prospects in Cr(VI) and BPA removal. In addition, the combination of MIL-100(Fe) and WO_3 can enhance the photocatalysis and photo-Fenton performances, which open a new door to provide an alternative photocatalysts to accomplish improved removal of pollutants for clean production and environmental sustainability.

CRediT authorship contribution statement

Jia-Wei Wang: Data curation, Investigation, Visualization, Writing - original draft. **Fu-Guo Qiu:** Resources, Validation. **Peng Wang:** Resources. **Chengjun Ge:** Resources. **Chong-Chen Wang:** Conceptualization, Funding acquisition, Supervision, Project administration, Writing - review & editing.

Declaration of competing interest

The authors declare that they have no known competing financial interests or personal relationships that could have appeared to influence the work reported in this paper.

Acknowledgements

This work was supported by National Natural Science Foundation of China (51878023), Beijing Natural Science Foundation (No.8202016), Great Wall Scholars Training Program Project of Beijing Municipality Universities (CIT&TCD20180323), and Beijing Talent Project (2019A22).

Appendix A. Supplementary data

Supplementary data to this article can be found online at https://doi.org/10.1016/j.jclepro.2020.123408.

References

Abdpour, S., Kowsari, E., Alavi Moghaddam, M.R., Schmolke, L., Janiak, C., 2018. Mil-100(Fe) nanoparticles supported on urchin like Bi_2S_3 structure for improving photocatalytic degradation of rhodamine-B dye under visible light irradiation. J. Solid State Chem. 266, 54–62. https://doi.org/10.1016/j.jssc.2018.07.006.

Ahmad, M., Chen, S., Ye, F., Quan, X., Afzal, S., Yu, H., Zhao, X., 2019. Efficient photo-Fenton activity in mesoporous MIL-100(Fe) decorated with ZnO nanosphere for pollutants degradation. Appl. Catal. B Environ. 245, 428–438. https://doi.org/10.1016/j.apcatb.2018.12.057.

Ai, L., Zhang, C., Li, L., Jiang, J., 2014. Iron terephthalate metal–organic framework: revealing the effective activation of hydrogen peroxide for the degradation of organic dye under visible light irradiation. Appl. Catal. B Environ. 148–149, 191–200. https://doi.org/10.1016/j.apcatb.2013.10.056.

Awual, M.R., Hasan, M.M., Islam, A., Rahman, M.M., Asiri, A.M., Khaleque, M.A., Sheikh, M.C., 2019. Offering an innovative composited material for effective lead(II) monitoring and removal from polluted water. J. Clean. Prod. 231, 214–223. https://doi.org/10.1016/j.jclepro.2019.05.125.

Baeck, S.H., Choi, K.S., Jaramillo, T.F., Stucky, G.D., McFarland, E.W., 2003. Enhancement of photocatalytic and electrochromic properties of electrochemically fabricated mesoporous WO_3 thin films. Adv. Mater. 15, 1269–1273. https://doi.org/10.1002/adma.200304669.

Barrera-Diaz, C.E., Lugo-Lugo, V., Bilyeu, B., 2012. A review of chemical, electrochemical and biological methods for aqueous Cr(VI) reduction. J. Hazard Mater. 223–224, 1–12. https://doi.org/10.1016/j.jhazmat.2012.04.054.

Buaisha, M., Balku, S., Yaman, Ş.Ö., 2020. Heavy metal removal investigation in conventional activated sludge systems. Civil Engineering Journal 6, 470–477. https://doi.org/10.28991/cej-2020-03091484.

Castro, L., Dedryvère, R., Ledeuil, J.B., Bréger, J., Tessier, C., Gonbeau, D., 2012. Aging mechanisms of $LiFePO_4$//graphite cells studied by XPS: redox reaction and electrode/electrolyte interfaces. J. Electrochem. Soc. 159, A357–A363. https://doi.org/10.1149/2.024204jes.

Chen, D.-D., Yi, X.-H., Zhao, C., Fu, H., Wang, P., Wang, C.-C., 2020. Polyaniline modified MIL-100(Fe) for enhanced photocatalytic Cr(VI) reduction and tetracycline degradation under white light. Chemosphere 245, 125659. https://doi.org/10.1016/j.chemosphere.2019.125659.

Chen, G., Li, D., Li, F., Fan, Y., Zhao, H., Luo, Y., Yu, R., Meng, Q., 2012. Ball-milling combined calcination synthesis of MoS_2/CdS photocatalysts for high photocatalytic H_2 evolution activity under visible light irradiation. Appl. Catal. Gen. 443–444, 138–144. https://doi.org/10.1016/j.apcata.2012.07.033.

Chen, Q., Wu, P., Li, Y., Zhu, N., Dang, Z., 2009. Heterogeneous photo-Fenton photodegradation of reactive brilliant orange X-GN over iron-pillared montmorillonite under visible irradiation. J. Hazard Mater. 168, 901–908. https://doi.org/10.1016/j.jhazmat.2009.02.107.

Chen, S., Hu, Y., Meng, S., Fu, X., 2014. Study on the separation mechanisms of photogenerated electrons and holes for composite photocatalysts g-C_3N_4-WO_3. Appl. Catal. B Environ. 150–151, 564–573. https://doi.org/10.1016/j.apcatb.2013.12.053.

Cheng, M., Lai, C., Liu, Y., Zeng, G., Huang, D., Zhang, C., Qin, L., Hu, L., Zhou, C., Xiong, W., 2018. Metal-organic frameworks for highly efficient heterogeneous Fenton-like catalysis. Coord. Chem. Rev. 368, 80–92. https://doi.org/10.1016/j.ccr.2018.04.012.

Debnath, A., Majumder, M., Pal, M., Das, N.S., Chattopadhyay, K.K., Saha, B., 2016. Enhanced adsorption of hexavalent chromium onto magnetic calcium ferrite nanoparticles: kinetic, isotherm, and neural network modeling. J. Dispersion Sci. Technol. 37, 1806–1818. https://doi.org/10.1080/01932691.2016.1141100.

Du, X., Yi, X., Wang, P., Deng, J., Wang, C.-c., 2019. Enhanced photocatalytic Cr(VI) reduction and diclofenac sodium degradation under simulated sunlight irradiation over MIL-100(Fe)/g-C_3N_4 heterojunctions. Chin. J. Catal. 40, 70–79. https://doi.org/10.1016/S1872-2067(18)63160-2.

Fakhri, H., Bagheri, H., 2020. Highly efficient Zr-MOF@WO_3/graphene oxide photocatalyst: synthesis, characterization and photodegradation of tetracycline and malathion. Mater. Sci. Semicond. Process. 107, 104815. https://doi.org/10.1016/j.mssp.2019.104815.

Feng, M., Liu, Y., Zhao, Z., Huang, H., Peng, Z., 2019. The preparation of Fe doped triclinic-hexagonal phase heterojunction WO_3 film and its enhanced photocatalytic reduction of Cr (VI). Mater. Res. Bull. 109, 168–174. https://doi.org/10.1016/j.materresbull.2018.05.007.

Fu, J., Xu, Q., Low, J., Jiang, C., Yu, J., 2019. Ultrathin 2D/2D WO_3/g-C_3N_4 step-scheme H_2 production photocatalyst. Appl. Catal. B Environ. 243, 556–565. https://doi.org/10.1016/j.apcatb.2018.11.011.

Gao, C., Chen, S., Quan, X., Yu, H., Zhang, Y., 2017. Enhanced Fenton-like catalysis by iron-based metal organic frameworks for degradation of organic pollutants. J. Catal. 356, 125–132. https://doi.org/10.1016/j.jcat.2017.09.015.

Gong, Y., Yang, B., Zhang, H., Zhao, X., 2018. A g-C_3N_4/MIL-101(Fe) heterostructure composite for highly efficient BPA degradation with persulfate under visible light irradiation. J. Mater. Chem. 6, 23703–23711. https://doi.org/10.1039/C8TA07915C.

Guo, T., Wang, K., Zhang, G., Wu, X., 2019. A novel α-Fe_2O_3@g-C_3N_4 catalyst: synthesis derived from Fe-based MOF and its superior photo-Fenton performance. Appl. Surf. Sci. 469, 331–339. https://doi.org/10.1016/j.apsusc.2018.10.183.

Huang, W., Liu, N., Zhang, X., Wu, M., Tang, L., 2017. Metal organic framework g-C_3N_4/MIL-53(Fe) heterojunctions with enhanced photocatalytic activity for Cr(VI) reduction under visible light. Appl. Surf. Sci. 425, 107–116. https://doi.org/10.1016/j.apsusc.2017.07.050.

Huo, S.-H., Yan, X.-P., 2012. Metal–organic framework MIL-100(Fe) for the adsorption of malachite green from aqueous solution. J. Mater. Chem. 22, 7449–7455. https://doi.org/10.1039/C2JM16513A.

Jiang, W., Qu, D., An, L., Gao, X., Wen, Y., Wang, X., Sun, Z., 2019. Deliberate construction of direct Z-scheme photocatalysts through photodeposition. J. Mater. Chem. 7, 18348–18356. https://doi.org/10.1039/c9ta05607f.

Jiang, W., Zong, X., An, L., Hua, S., Miao, X., Luan, S., Wen, Y., Tao, F.F., Sun, Z., 2018. Consciously constructing heterojunction or direct Z-scheme photocatalysts by regulating electron flow direction. ACS Catal. 8, 2209–2217. https://doi.org/10.1021/acscatal.7b04323.

Li, M., Liu, Y., Shen, C., Li, F., Wang, C.-C., Huang, M., Yang, B., Wang, Z., Yang, J., Sand, W., 2019. One-step Sb(III) decontamination using a bifunctional photoelectrochemical filter. J. Hazard Mater. 389, 121840. https://doi.org/10.1016/j.jhazmat.2019.121840.

Liang, R., Jing, F., Shen, L., Qin, N., Wu, L., 2015a. MIL-53(Fe) as a highly efficient bifunctional photocatalyst for the simultaneous reduction of Cr(VI) and oxidation of dyes. J. Hazard Mater. 287, 364–372. https://doi.org/10.1016/j.jhazmat.2015.01.048.

Liang, R., Luo, S., Jing, F., Shen, L., Qin, N., Wu, L., 2015b. A simple strategy for fabrication of Pd@MIL-100(Fe) nanocomposite as a visible-light-driven photocatalyst for the treatment of pharmaceuticals and personal care products (PPCPs). Appl. Catal. B Environ. 176–177, 240–248. https://doi.org/10.1016/j.apcatb.2015.04.009.

Liang, R., Shen, L., Jing, F., Wu, W., Qin, N., Lin, R., Wu, L., 2015c. NH_2-mediated indium metal–organic framework as a novel visible-light-driven photocatalyst for reduction of the aqueous Cr(VI). Appl. Catal. B Environ. 162, 245–251. https://doi.org/10.1016/j.apcatb.2014.06.049.

Lima, L.V.C., Rodriguez, M., Freitas, V.A.A., Souza, T.E., Machado, A.E.H., Patrocínio, A.O.T., Fabris, J.D., Oliveira, L.C.A., Pereira, M.C., 2015. Synergism between n-type WO_3 and p-type δ-FeOOH semiconductors: high interfacial contacts and enhanced photocatalysis. Appl. Catal. B Environ. 165, 579–588. https://doi.org/10.1016/j.apcatb.2014.10.066.

Lin, J., Hu, Y., Wang, L., Liang, D., Ruan, X., Shao, S., 2020. M88/PS/Vis system for degradation of bisphenol A: environmental factors, degradation pathways, and toxicity evaluation. Chem. Eng. J. 382, 122931. https://doi.org/10.1016/j.cej.2019.122931.

Liu, B., Wu, Y., Han, X., Lv, J., Zhang, J., Shi, H., 2018. Facile synthesis of g-C_3N_4/amine-functionalized MIL-101(Fe) composites with efficient photocatalytic activities under visible light irradiation. J. Mater. Sci. Mater. Electron. 29, 17591–17601. https://doi.org/10.1007/s10854-018-9862-x.

Liu, X., Yan, Y., Da, Z., Shi, W., Ma, C., Lv, P., Tang, Y., Yao, G., Wu, Y., Huo, P., Yan, Y., 2014. Significantly enhanced photocatalytic performance of CdS coupled WO_3 nanosheets and the mechanism study. Chem. Eng. J. 241, 243–250. https://doi.org/10.1016/j.cej.2013.12.058.

Liu, X., Zhou, H., Pei, S., Xie, S., You, S., 2020. Oxygen-deficient WO_3−x nanoplate array film photoanode for efficient photoelectrocatalytic water decontamination. Chem. Eng. J. 381, 122740. https://doi.org/10.1016/j.cej.2019.122740.

Lv, H., Zhao, H., Cao, T., Qian, L., Wang, Y., Zhao, G., 2015. Efficient degradation of high concentration azo-dye wastewater by heterogeneous Fenton process with iron-based metal-organic framework. J. Mol. Catal. Chem. 400, 81–89. https://doi.org/10.1016/j.molcata.2015.02.007.

Malik, A., Nath, M., 2019. Multicore–shell nanocomposite formed by encapsulation of WO_3 in zeolitic imidazolate framework (ZIF-8): as an efficient photocatalyst. J. Environ. Chem. Eng. 7, 103401. https://doi.org/10.1016/j.jece.2019.103401.

Meng, L., Gan, L., Gong, H., Su, J., Wang, P., Li, W., Chu, W., Xu, L., 2019. Efficient degradation of bisphenol A using High-Frequency Ultrasound: analysis of influencing factors and mechanistic investigation. J. Clean. Prod. 232, 1195–1203. https://doi.org/10.1016/j.jclepro.2019.06.055.

Molkenthin, M., Olmez-Hanci, T., Jekel, M.R., Arslan-Alaton, I., 2013. Photo-Fenton-like treatment of BPA: effect of UV light source and water matrix on toxicity and transformation products. Water Res. 47, 5052–5064. https://doi.org/10.1016/j.watres.2013.05.051.

Niu, Z., Qiu, C., Jiang, J., Ai, L., 2018. Hierarchical CoP–FeP branched heterostructures for highly efficient electrocatalytic water splitting. ACS Sustain. Chem. Eng. 7, 2335–2342. https://doi.org/10.1021/acssuschemeng.8b05089.

Oladipo, A.A., 2018. MIL-53 (Fe)-based photo-sensitive composite for degradation of organochlorinated herbicide and enhanced reduction of Cr(VI). Process Saf. Environ. Protect. 116, 413–423. https://doi.org/10.1016/j.psep.2018.03.011.

Qiu, J., Zhang, X., Feng, Y., Zhang, X., Wang, H., Yao, J., 2018. Modified metal-organic frameworks as photocatalysts. Appl. Catal. B Environ. 231, 317–342. https://doi.org/10.1016/j.apcatb.2018.03.039.

Sharma, J., Mishra, I.M., Dionysiou, D.D., Kumar, V., 2015. Oxidative removal of Bisphenol A by UV-C/peroxymonosulfate (PMS): kinetics, influence of co-existing chemicals and degradation pathway. Chem. Eng. J. 276, 193–204. https://doi.org/10.1016/j.cej.2015.04.021.

Shi, L., Wang, T., Zhang, H., Chang, K., Meng, X., Liu, H., Ye, J., 2015. An amine-functionalized iron(III) metal-organic framework as efficient visible-light photocatalyst for Cr(VI) reduction. Adv. Sci. 2, 1500006. https://doi.org/10.1002/advs.201500006.

Song, G., Wang, Z., Wang, L., Li, G., Huang, M., Yin, F., 2014. Preparation of MOF(Fe) and its catalytic activity for oxygen reduction reaction in an alkaline electrolyte. Chin. J. Catal. 35, 185–195. https://doi.org/10.1016/s1872-2067(12)60729-3.

Su, Y., Han, Z., Zhang, L., Wang, W., Duan, M., Li, X., Zheng, Y., Wang, Y., Lei, X., 2017. Surface hydrogen bonds assisted meso-porous WO_3 photocatalysts for high selective oxidation of benzylalcohol to benzylaldehyde. Appl. Catal. B Environ. 217, 108–114. https://doi.org/10.1016/j.apcatb.2017.05.075.

Sun, D., Liu, W., Fu, Y., Fang, Z., Sun, F., Fu, X., Zhang, Y., Li, Z., 2014. Noble metals can have different effects on photocatalysis over metal–organic frameworks (MOFs): a case study on M/NH_2-MIL-125(Ti) (M=Pt and Au). Chem. Eur J. 20, 4780–4788. https://doi.org/10.1002/chem.201304067.

Tang, J., Wang, J., 2019. Iron-copper bimetallic metal-organic frameworks for efficient Fenton-like degradation of sulfamethoxazole under mild conditions. Chemosphere 241, 125002. https://doi.org/10.1016/j.chemosphere.2019.125002.

Teo, S.H., Islam, A., Chan, E.S., Thomas Choong, S.Y., Alharthi, N.H., Taufiq-Yap, Y.H., Awual, M.R., 2019. Efficient biodiesel production from Jatropha curcus using $CaSO_4$/Fe_2O_3-SiO_2 core-shell magnetic nanoparticles. J. Clean. Prod. 208, 816–826. https://doi.org/10.1016/j.jclepro.2018.10.107.

Theingi, M., Tun, K.T., Aung, N.N., 2019. Preparation, characterization and optical property of $LaFeO_3$ nanoparticles via sol-gel combustion method. SciMedicine Journal 1, 151–157. https://doi.org/10.28991/SciMedJ-2019-0103-5.

Vignesh, K., Priyanka, R., Rajarajan, M., Suganthi, A., 2013. Photoreduction of Cr(VI) in water using Bi_2O_3–ZrO_2 nanocomposite under visible light irradiation. Mater. Sci. Eng., B 178, 149–157. https://doi.org/10.1016/j.mseb.2012.10.035.

Wang, C.-C., Li, J.-R., Lv, X.-L., Zhang, Y.-Q., Guo, G., 2014. Photocatalytic organic pollutants degradation in metal–organic frameworks. Energy Environ. Sci. 7, 2831–2867. https://doi.org/10.1039/C4EE01299B.

Wang, C.-C., Wang, X., Liu, W., 2019a. The synthesis strategies and photocatalytic performances of TiO_2/MOFs composites: a state-of-the-art review. Chem. Eng. J. 391, 123601. https://doi.org/10.1016/j.cej.2019.123601.

Wang, C.-C., Yi, X.-H., Wang, P., 2019b. Powerful combination of MOFs and C_3N_4 for enhanced photocatalytic performance. Appl. Catal. B Environ. 247, 24–48. https://doi.org/10.1016/j.apcatb.2019.01.091.

Wang, C., Zhu, L., Wei, M., Chen, P., Shan, G., 2012. Photolytic reaction mechanism and impacts of coexisting substances on photodegradation of bisphenol A by Bi_2WO_6 in water. Water Res. 46, 845–853. https://doi.org/10.1016/j.watres.2011.11.057.

Wang, D., Jia, F., Wang, H., Chen, F., Fang, Y., Dong, W., Zeng, G., Li, X., Yang, Q.,

Yuan, X., 2018. Simultaneously efficient adsorption and photocatalytic degradation of tetracycline by Fe-based MOFs. J. Colloid Interface Sci. 519, 273–284. https://doi.org/10.1016/j.jcis.2018.02.067.

Wang, H., Yuan, X., Wu, Y., Zeng, G., Chen, X., Leng, L., Wu, Z., Jiang, L., Li, H., 2015. Facile synthesis of amino-functionalized titanium metal-organic frameworks and their superior visible-light photocatalytic activity for Cr(VI) reduction. J. Hazard Mater. 286, 187–194. https://doi.org/10.1016/j.jhazmat.2014.11.039.

Wang, J., Lee, P.S., Ma, J., 2009. Synthesis, growth mechanism and room-temperature blue luminescence emission of uniform WO_3 nanosheets with W as starting material. J. Cryst. Growth 311, 316–319. https://doi.org/10.1016/j.jcrysgro.2008.11.016.

Wang, J.C., Ren, J., Yao, H.C., Zhang, L., Wang, J.S., Zang, S.Q., Han, L.F., Li, Z.J., 2016. Synergistic photocatalysis of Cr(VI) reduction and 4-Chlorophenol degradation over hydroxylated alpha-Fe_2O_3 under visible light irradiation. J. Hazard Mater. 311, 11–19. https://doi.org/10.1016/j.jhazmat.2016.02.055.

Wang, S., Wang, X., 2015. Multifunctional metal–organic frameworks for photocatalysis. Small 11, 3097–3112. https://doi.org/10.1002/smll.201500084.

Wu, L., Hong, J., Zhang, Q., Chen, B.-Y., Wang, J., Dong, Z., 2020. Deciphering highly resistant characteristics to different pHs of oxygen vacancy-rich Fe_2Co_1-LDH/PS system for bisphenol A degradation. Chem. Eng. J. 385, 123620. https://doi.org/10.1016/j.cej.2019.123620.

Xin, Y., Gao, M., Wang, Y., Ma, D., 2014. Photoelectrocatalytic degradation of 4-nonylphenol in water with WO_3/TiO_2 nanotube array photoelectrodes. Chem. Eng. J. 242, 162–169. https://doi.org/10.1016/j.cej.2013.12.068.

Xu, B., Chen, Z., Han, B., Li, C., 2017. Glycol assisted synthesis of MIL-100(Fe) nanospheres for photocatalytic oxidation of benzene to phenol. Catal. Commun. 98, 112–115. https://doi.org/10.1016/j.catcom.2017.04.041.

Xu, L., Wang, J., 2011. A heterogeneous Fenton-like system with nanoparticulate zero-valent iron for removal of 4-chloro-3-methyl phenol. J. Hazard Mater. 186, 256–264. https://doi.org/10.1016/j.jhazmat.2010.10.116.

Ye, Y., Yang, H., Wang, X., Feng, W., 2018. Photocatalytic, Fenton and photo-Fenton degradation of RhB over Z-scheme g-C_3N_4/$LaFeO_3$ heterojunction photocatalysts. Mater. Sci. Semicond. Process. 82, 14–24. https://doi.org/10.1016/j.mssp.2018.03.033.

Yi, X.-H., Ma, S.-Q., Du, X.-D., Zhao, C., Fu, H., Wang, P., Wang, C.-C., 2019b. The facile fabrication of 2D/3D Z-scheme g-C_3N_4/UiO-66 heterojunction with enhanced photocatalytic Cr(VI) reduction performance under white light. Chem. Eng. J. 375, 121944. https://doi.org/10.1016/j.cej.2019.121944.

Yu, W., Xu, D., Peng, T., 2015. Enhanced photocatalytic activity of g-C_3N_4 for selective CO_2 reduction to CH_3OH via facile coupling of ZnO: a direct Z-scheme mechanism. J. Mater. Chem. 3, 19936–19947. https://doi.org/10.1039/c5ta05503b.

Žerjav, G., Arshad, M.S., Djinović, P., Zavašnik, J., Pintar, A., 2017. Electron trapping energy states of TiO_2–WO_3 composites and their influence on photocatalytic degradation of bisphenol A. Appl. Catal. B Environ. 209, 273–284. https://doi.org/10.1016/j.apcatb.2017.02.059.

Zhang, J., Liu, X., Wang, X., Mu, L., Yuan, M., Liu, B., Shi, H., 2018. Carbon dots-decorated $Na_2W_4O_{13}$ composite with WO_3 for highly efficient photocatalytic antibacterial activity. J. Hazard Mater. 359, 1–8. https://doi.org/10.1016/j.jhazmat.2018.06.072.

Zhang, J., Ma, H., Liu, Z., 2017. Highly efficient photocatalyst based on all oxides WO_3/Cu_2O heterojunction for photoelectrochemical water splitting. Appl. Catal. B Environ. 201, 84–91. https://doi.org/10.1016/j.apcatb.2016.08.025.

Zhang, L., Wang, W., Sun, S., Sun, Y., Gao, E., Zhang, Z., 2014. Elimination of BPA endocrine disruptor by magnetic BiOBr@SiO_2@Fe_3O_4 photocatalyst. Appl. Catal. B Environ. 148–149, 164–169. https://doi.org/10.1016/j.apcatb.2013.10.053.

Zhang, S., Zhao, X., Niu, H., Shi, Y., Cai, Y., Jiang, G., 2009. Superparamagnetic Fe_3O_4 nanoparticles as catalysts for the catalytic oxidation of phenolic and aniline compounds. J. Hazard Mater. 167, 560–566. https://doi.org/10.1016/j.jhazmat.2009.01.024.

Zhao, C., Wang, Z., Li, X., Yi, X., Chu, H., Chen, X., Wang, C.-C., 2019. Facile fabrication of BUC-21/$Bi_{24}O_{31}Br_{10}$ composites for enhanced photocatalytic Cr(VI) reduction under white light. Chem. Eng. J. 389, 123431. https://doi.org/10.1016/j.cej.2019.123431.

Zhao, Z., An, H., Lin, J., Feng, M., Murugadoss, V., Ding, T., Liu, H., Shao, Q., Mai, X., Wang, N., Gu, H., Angaiah, S., Guo, Z., 2019. Progress on the photocatalytic reduction removal of chromium contamination. Chem. Rec. 19, 873–882. https://doi.org/10.1002/tcr.201800153.

Zhou, Y.-C., Xu, X.-Y., Wang, P., Fu, H., Zhao, C., Wang, C.-C., 2019. Facile fabrication and enhanced photocatalytic performance of visible light responsive UiO-66-NH_2/Ag_2CO_3 composite. Chin. J. Catal. 40, 1912–1923. https://doi.org/10.1016/S1872-2067(19)63433-9.

Zhou, Y., Zhou, T., Zhang, Y., Tang, L., Guo, Q., Wang, M., Xie, C., Zeng, D., 2020. Synthesis of core-shell flower-like WO_3@ZIF-71 with enhanced response and selectivity to H_2S gas. Solid State Ionics 350, 115278. https://doi.org/10.1016/j.ssi.2020.115278.

Zhu, Y., Zhu, R., Xi, Y., Xu, T., Yan, L., Zhu, J., Zhu, G., He, H., 2018. Heterogeneous photo-Fenton degradation of bisphenol A over Ag/AgCl/ferrihydrite catalysts under visible light. Chem. Eng. J. 346, 567–577. https://doi.org/10.1016/j.cej.2018.04.073.